




Dynamical detection of mean-field topological phases in an interacting Chern insulatorWei Jia ^{1,2} Long Zhang,^{3,1,2} Lin Zhang ^{4,1,2} and Xiong-Jun Liu ^{1,2,5,6,*}¹*International Center for Quantum Materials and School of Physics, Peking University, Beijing 100871, China*²*Hefei National Laboratory, Hefei 230088, China*³*School of Physics and Institute for Quantum Science and Engineering, Huazhong University of Science and Technology, Wuhan 430074, China*⁴*ICFO-Institut de Ciències Fòniques, The Barcelona Institute of Science and Technology, Av. Carl Friedrich Gauss 3, 08860 Castelldefels (Barcelona), Spain*⁵*CAS Center for Excellence in Topological Quantum Computation, University of Chinese Academy of Sciences, Beijing 100190, China*⁶*International Quantum Academy, Shenzhen 518048, China*

(Received 26 June 2022; revised 4 January 2023; accepted 28 February 2023; published 15 March 2023)

Interactions generically have important effects on topological quantum phases. For a quantum anomalous Hall (QAH) insulator, the presence of interactions can qualitatively change a topological phase diagram, which, however, is typically hard to measure in an experiment. Here we propose a scheme based on quench dynamics to detect the mean-field topological phase diagram of an interacting Chern insulator described by the QAH-Hubbard model, with nontrivial dynamical quantum physics being uncovered. We focus on the dynamical properties of the system at a weak to intermediate Hubbard interaction, which mainly induces a ferromagnetic order under the mean-field level. Remarkably, three characteristic times— t_s , t_c , and t^* —are found in the quench dynamics. The first two (t_s , t_c) capture the emergences of dynamical self-consistent particle density and the dynamical topological phase transition, respectively, while the third one (t^*) gives a linear scaling time on the topological phase boundaries. We show generically that the characteristic times obey $t_s > t^* > t_c$ ($t^* < t_s < t_c$) in the repulsive (attractive) interacting regime, when the system is quenched from an initial nearly fully polarized state to the topologically nontrivial regimes. Moreover, the Chern number of the equilibrium phase of postquench interacting Hamiltonian can be determined by any two of the three timescales, providing a dynamical way to determine the equilibrium mean-field topological phases. Experimentally, the measurement of t_s is challenging, while t_c and t^* can be directly read out by measuring the spin polarizations of four Dirac points and the time-dependent particle density, respectively, showing the feasibility of the present dynamical scheme. Our work opens a way to detect by quench dynamics the mean-field phase diagram of Chern insulators with interactions.

DOI: [10.1103/PhysRevB.107.125132](https://doi.org/10.1103/PhysRevB.107.125132)**I. INTRODUCTION**

Topological quantum phases are currently a focus of research in condensed-matter physics [1–5]. At equilibrium, the topological phases can be characterized by nonlocal topological invariants [6,7] defined in ground states. This classifies the gapped band structures into distinct topological states, with great success having been achieved in the study of topological insulators [8–11], topological semimetals [12–15], and topological superconductors [16–20]. Nevertheless, this non-interacting topological phase can be greatly affected after considering many-body interaction [21–32]. For instance, a repulsive Hubbard interaction can drive a trivial insulator into a topological Mott insulator [33–35], while an attractive Hubbard interaction may drive a trivial phase of a two-dimensional (2D) quantum anomalous Hall (QAH) system into a topological superconductor/superfluid [36–39]. Hence it is still a fundamental issue, and is usually difficult in experiments, to accurately identify the topological phases driven by the interactions.

In recent years, the rapid development of quantum simulations [40–42] has provided new realistic platforms to explore exotic interacting physics, such as ultracold atoms in optical lattices [43–49] and superconducting qubits [50–52]. A number of topological models have been realized in experiments, such as the 1D Su-Schrieffer-Heeger model [53,54], a 1D AIII class topological insulator [55,56], 1D bosonic symmetry-protected phase [57,58], the 2D Haldane model [59], the spin-orbit coupled QAH model [60–62], and the 3D Weyl semimetal band [63–67]. Accordingly, various detection schemes for exotic topological physics have also been developed, ranging from measurements of equilibrium topological physics [68–71] to nonequilibrium quantum dynamics [72–81]. In particular, dynamical characterization [82–88] shows the correspondence between broad classes of equilibrium topological phases and the emergent dynamical topology in far-from-equilibrium quantum dynamics induced by quenching such topological systems, which brings about systematic and high-precision schemes to detect topological phases based on quantum dynamics, and it has advanced broad studies in experiment [89–98]. Nevertheless, these current studies have focused mainly on noninteracting topological systems, while particle-particle interactions are expected to

*Corresponding author: xiongjunliu@pku.edu.cn

have crucial effects on the topological phases, the detection of which is typically hard to achieve. For example, when quenching an interacting topological system [99–102], both the interactions and the many-body states of the system evolve simultaneously after quenching, leading to complex nonlinear quantum dynamics [103–106] and exotic nonequilibrium phenomena [107–110]. With the above considerations, there are two nontrivial issues for quantum dynamics in the interacting Chern insulator that have not been studied: (i) How do the dynamical properties change when the Hubbard interaction is added into the Chern insulator while performing quench dynamics? (ii) Is there any universal feature in the dynamical evolution to characterize the equilibrium mean-field topological phases?

We address these issues in this paper, and we propose a scheme based on quench dynamics to detect the mean-field topological phase diagram of an interacting Chern insulator described by the QAH-Hubbard model, with nontrivial dynamical quantum physics being uncovered. Specifically, we consider a 2D QAH system in the presence of a weak to intermediate Hubbard interaction, which mainly induces a ferromagnetic order under the mean-field level. By quenching the system from an initial nearly fully polarized trivial state to a parameter regime in which the equilibrium phase is topologically nontrivial, we uncover two dynamical phenomena rendering the dynamical signals of the equilibrium mean-field phase. First, there are three characteristic times— t_s , t_c , and t^* —capturing the dynamical self-consistent particle density, the dynamical topological phase transition, and the linear scaling time on the topological phase boundaries, respectively. Second, $t_s > t^* > t_c$ ($t^* < t_s < t_c$) occurs in the repulsive (attractive) interaction, and the Chern number is determined by any two characteristic timescales. Based on these two fundamental properties, we can easily determine the equilibrium mean-field topological phase diagram by comparing any two timescales. Experimentally, the measurement of t_s is challenging while t_c and t^* can be directly read out by measuring the spin polarizations of four Dirac points and the time-dependent particle density, respectively. This result provides a dynamical detection scheme with high feasibility and simplicity for measuring the mean-field topological phase diagram in interacting systems, which may be applied to recent quantum simulation experiments.

The remaining part of this paper is organized as follows. In Sec. II, we introduce the QAH-Hubbard model. In Sec. III, we study the quench dynamics of the system. In Sec. IV, we reveal the nontrivial dynamical properties in quench dynamics. In Sec. V, we determine the mean-field topological phase diagram via the timescales. In Sec. VI, we propose the experimental detection scheme for the equilibrium mean-field topological phases. Finally, we summarize the main results and provide a brief discussion in Sec. VII.

II. QAH-HUBBARD MODEL

Our starting point is a minimal 2D QAH model [36,38], which has recently been realized in cold atoms [60,62,89,91], together with an attractive or repulsive on-site Hubbard interaction of strength U . The system is now described by the

QAH-Hubbard Hamiltonian

$$\begin{aligned} H &= \sum_{\mathbf{k}} C_{\mathbf{k}}^\dagger \mathcal{H}_{\mathbf{k}}^{(0)} C_{\mathbf{k}} + U \sum_{\mathbf{j}} n_{\mathbf{j}\uparrow} n_{\mathbf{j}\downarrow}, \quad \mathcal{H}_{\mathbf{k}}^{(0)} = \mathbf{h}_{\mathbf{k}} \cdot \boldsymbol{\sigma} \\ &= [m_z - 2t_0(\cos k_x + \cos k_y)]\sigma_z \\ &\quad + 2t_{s_0} \sin k_y \sigma_x + 2t_{s_0} \sin k_x \sigma_y, \end{aligned} \quad (1)$$

where $C_{\mathbf{k}} = (c_{\mathbf{k}\uparrow}, c_{\mathbf{k}\downarrow})^T$ is the spinor operator of momentum \mathbf{k} , $n_{\mathbf{j}s} = c_{\mathbf{j}s}^\dagger c_{\mathbf{j}s}$ with $s = \uparrow$ or \downarrow is the particle number operator at site \mathbf{j} , $\sigma_{x,y,z}$ are the Pauli matrices, and m_z is the Zeeman coupling. Here t_0 and t_{s_0} are the spin-conserved and spin-flipped hopping coefficients, respectively. In the noninteracting case, the Bloch Hamiltonian $\mathcal{H}_{\mathbf{k}}^{(0)}$ produces two energy bands $\pm e_{\mathbf{k}} = \pm \sqrt{h_{x,\mathbf{k}}^2 + h_{y,\mathbf{k}}^2 + h_{z,\mathbf{k}}^2}$, for which the gap can be closed at Dirac points $\mathbf{D}_i \in \{\mathbf{X}_1, \mathbf{X}_2, \boldsymbol{\Gamma}, \mathbf{M}\}$ with $\mathbf{X}_1 = (0, \pi)$, $\mathbf{X}_2 = (\pi, 0)$, $\boldsymbol{\Gamma} = (0, 0)$, and $\mathbf{M} = (\pi, \pi)$ for certain Zeeman coupling. When the system is fully gapped, the corresponding band topology can be characterized by the first Chern number Ch_1 , determining the QAH topological region $0 < |m_z| < 4t_0$ with $\text{Ch}_1 = \text{sgn}(m_z)$ and the trivial region $|m_z| > 4t_0$. This noninteracting topological property can also be captured by the intuitive physical quantities, such as the numbers of edge states [36], the spin textures on band inversion surfaces [82,91], and the spin polarizations at four Dirac points [60,68].

The presence of nonzero interactions can greatly affect the physics of Hamiltonian (1) and may induce various interesting quantum phases at suitable interaction strength, such as the superfluid phase in attractive interaction [111,112] and the antiferromagnetic phase in repulsive interaction [113,114]. Especially for a general strong interaction, the system may host rich magnetic phases [115–117]. Here we focus on the 2D system at half-filling within a weak to intermediate interacting regime, where the interaction mainly induces ferromagnetic order [118]. For this 2D case, the Hubbard interaction can be still treated by employing the mean-field theory, in which the fluctuations around the average value of the order parameter are small and can be neglected [37–39,104–106]. Accordingly, the Hubbard interaction term is rewritten as

$$\sum_{\mathbf{j}} n_{\mathbf{j}\uparrow} n_{\mathbf{j}\downarrow} = n_{\uparrow} \sum_{\mathbf{k}} c_{\mathbf{k}\downarrow}^\dagger c_{\mathbf{k}\downarrow} + n_{\downarrow} \sum_{\mathbf{k}} c_{\mathbf{k}\uparrow}^\dagger c_{\mathbf{k}\uparrow} - N n_{\uparrow} n_{\downarrow} \quad (2)$$

with $n_s = (1/N) \sum_{\mathbf{k}} \langle c_{\mathbf{k}s}^\dagger c_{\mathbf{k}s} \rangle$. Here N is the total number of sites. It is clear that the nonzero interaction corrects the Zeeman coupling to an effective form

$$m_z^{\text{eff}} = m_z - U \frac{(n_{\uparrow} - n_{\downarrow})}{2} = m_z - U n_d, \quad (3)$$

where $n_d \equiv (n_{\uparrow} - n_{\downarrow})/2$ is the difference of density for spin-up and spin-down particles. The effective Zeeman coupling shifts the topological region to $0 < |m_z^{\text{eff}}| < 4t_0$ with $\text{Ch}_1 = \text{sgn}(m_z^{\text{eff}})$ in the interacting regime.

By self-consistently calculating the particle density $n_{\uparrow(\downarrow)}$ [see Figs. 1(a) and 1(b)], the mean-field phase diagram of the QAH-Hubbard model (1) is shown in Fig. 1(c). An important feature is that the topological phase boundaries depend on the strength of nonzero interaction and the Zeeman coupling linearly (see Appendix A). Indeed, this linear behavior of topological boundaries is essentially a natural consequence

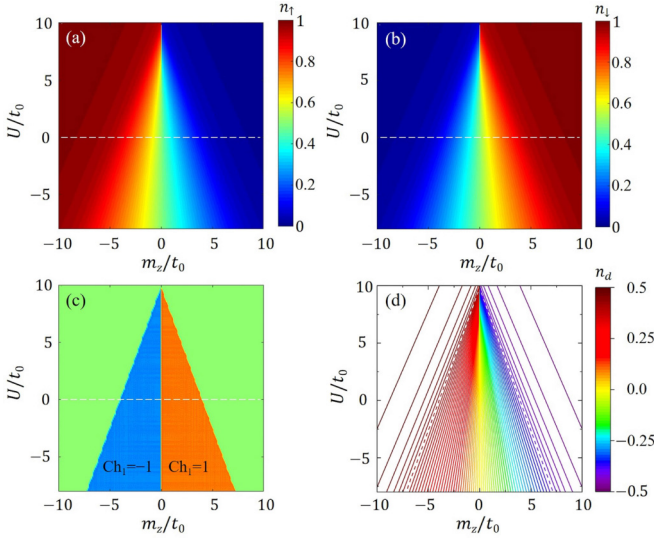


FIG. 1. (a),(b) Self-consistent results of n_\uparrow and n_\downarrow . (c) Mean-field phase diagram for the nonzero U and m_z . (d) Contour lines of n_d , where the topological phase boundaries (two dashed lines) have $n_d^* = \pm 0.4068$. Here we set $t_{so} = t_0$ and $N = 60 \times 60$.

of the linear form of the contour lines of n_d in terms of the interaction strength and Zeeman coupling, as we show in Fig. 1(d). On these lines, m_z^* is also unchanged, since n_d is fully determined by the effective Zeeman coupling. Specifically, we have $n_d^* = \pm 0.4068$ on the topological phase boundaries $|m_z^{\text{eff}}| = 4t_0$ for $t_{so} = t_0$. This linear scaling form of n_d greatly affects the dynamical properties of the system and leads to novel phenomena in the quench dynamics, as we show in Sec. IV.

III. QUENCH DYNAMICS

Quantum quench dynamics has been widely used in cold atoms [61,66,89,119]. We shall show that the above equilibrium mean-field phase diagram can be dynamically characterized and detected by employing the quantum quench scheme. Unlike the interaction quench in Refs. [103,105], here we choose the Zeeman coupling as the quench parameter, which has the following advantages: (i) The effective Zeeman coupling directly determines the topology of mean-field ground states at equilibrium; (ii) the Zeeman field in spin-orbit coupled quantum gases is controlled by the laser intensity and/or detuning and can be changed in a very short timescale, fulfilling the criterion for a sudden quench; and (iii) the realistic experiments [120–122] have demonstrated that both the magnitude and the sign of the Zeeman field can be tuned, which is more convenient to operate.

The quench protocol is as follows. First, we initialize the system into a nearly fully polarized state for time $t < 0$ by taking a very large constant magnetization $m_z^{(c)}$ along the σ_z axis but a very small $m_{x(y)}^{(c)}$ along the $\sigma_{x(y)}$ axis. In this case, the effect of interaction U can be ignored, and the spin of the initial state is almost along the z axis with only a very small component in the x - y plane. At $t = 0$, we suddenly change the Zeeman coupling $m_z^{(c)}$ to the postquenched value m_z and remove $m_{x(y)}^{(c)}$. Then, the nearly fully polarized state begins

to evolve under the equation of motion $i\dot{\Psi}_{\mathbf{k}}(t) = \mathcal{H}_{\mathbf{k}}(t)\Psi_{\mathbf{k}}(t)$ with the postquenched Hamiltonian

$$\mathcal{H}_{\mathbf{k}}(t) = \begin{bmatrix} h_{z,\mathbf{k}} + Un_\downarrow(t) & h_{x,\mathbf{k}} - ih_{y,\mathbf{k}} \\ h_{x,\mathbf{k}} + ih_{y,\mathbf{k}} & -h_{z,\mathbf{k}} + Un_\uparrow(t) \end{bmatrix}, \quad (4)$$

where $\Psi_{\mathbf{k}}(t) = [\chi_{\mathbf{k}}(t), \eta_{\mathbf{k}}(t)]^T$ is the instantaneous many-body state. We emphasize that $m_z^{(c)}$ should have the same sign as the postquenched m_z in order to facilitate the capture of nontrivial properties in quantum dynamics. Also, all the physics in the dynamics are robust against the tiny changes $|m_{x(y)}^{(c)}| \in [0, m_z]$ of the initial state.

Via the quench dynamics, we observe that the many-body state $\Psi_{\mathbf{k}}(t)$ and the postquenched Hamiltonian $\mathcal{H}_{\mathbf{k}}(t)$ are both time-evolved, where the instantaneous particle density is time-dependent and determined as

$$n_\uparrow(t) = \frac{1}{N} \sum_{\mathbf{k}} |\chi_{\mathbf{k}}(t)|^2, \quad n_\downarrow(t) = \frac{1}{N} \sum_{\mathbf{k}} |\eta_{\mathbf{k}}(t)|^2. \quad (5)$$

This dynamic behavior is completely different from the noninteracting quantum quenches, where the postquenched Hamiltonian remains unchanged [82–87]. Even if the postquenched Hamiltonian becomes steady after the long time evolution, it is still different from the equilibrium mean-field Hamiltonian with the postquenched m_z and U , i.e.,

$$\mathcal{H}_{\mathbf{k}}^{\text{MF}} = \begin{bmatrix} h_{z,\mathbf{k}} - Un_d + \frac{U}{2} & h_{x,\mathbf{k}} - ih_{y,\mathbf{k}} \\ h_{x,\mathbf{k}} + ih_{y,\mathbf{k}} & -h_{z,\mathbf{k}} + Un_d + \frac{U}{2} \end{bmatrix}. \quad (6)$$

Here n_d is the equilibrium value, as we show in Sec. II. Clearly, the novel dynamical evolution shows that the detection schemes for the noninteracting topological phases are inapplicable in this interacting case.

Next we employ the nontrivial characteristic time emerged in the above dynamical evolution to identify the mean-field topological phases. By defining the quantity $n_d(t) \equiv [n_\uparrow(t) - n_\downarrow(t)]/2$, the time-dependent effective Zeeman coupling is given by

$$m_z^{\text{eff}}(t) = m_z - Un_d(t). \quad (7)$$

Their dynamical properties are shown in Fig. 2, where $n_d(t)$ in a short-time evolution increases (decays) from an initial $n_d(t=0) \approx -0.5$ (0.5) when the postquenched Zeeman coupling is positive (negative). It should be noted that $m_z^{\text{eff}}(t)$ now determines the topological number $W(t)$ of postquenched Hamiltonian $\mathcal{H}_{\mathbf{k}}(t)$ through the relation $W(t) = \text{sgn}[m_z^{\text{eff}}(t)]$ for $0 < |m_z^{\text{eff}}(t)| < 4t_0$ and $W(t) = 0$ otherwise. Considering that the topology of equilibrium mean-field Hamiltonian (6) is actually determined by its self-consistent particle density $n_{\uparrow(\downarrow)}$, one idea for capturing the equilibrium mean-field topological phases is to find a characteristic time t_s in this dynamics such that

$$n_{\uparrow(\downarrow)}(t_s) = n_{\uparrow(\downarrow)}, \quad (8)$$

which gives a dynamical self-consistent particle density $n_{\uparrow(\downarrow)}(t_s)$ to characterize the equilibrium self-consistent particle density. Now this postquenched Hamiltonian at t_s is equivalent to the equilibrium mean-field Hamiltonian, and both of them host the same ground states. Accordingly, $m_z^{\text{eff}}(t_s)$ determines the topology of the equilibrium mean-field

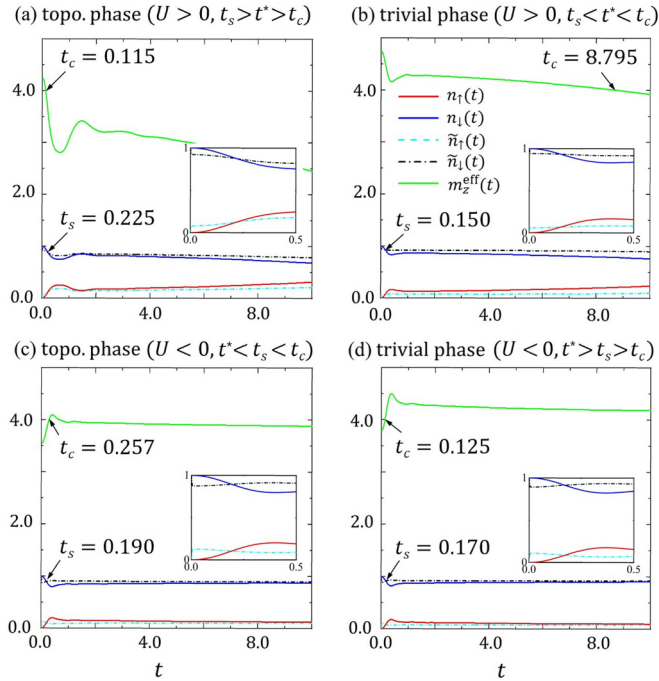


FIG. 2. Numerical results for $n_{\uparrow}(t)$ (red solid lines), $n_{\downarrow}(t)$ (blue solid lines), $m_z^{\text{eff}}(t)$ (green solid lines), $\tilde{n}_{\uparrow}(t)$ (light-blue dash-dotted lines), and $\tilde{n}_{\downarrow}(t)$ (black dash-dotted lines) for different interaction and equilibrium mean-field topological phases. Two characteristic times t_s and t_c emerge in the dynamical time evolution. Here the postquenched parameters are $(m_z, U) = (1.4, 5.7)$, $(3.0, 3.5)$, $(4.9, -2.7)$, and $(5.8, -4.0)$ for (a)–(d), respectively. The other characteristic time is $t^* = 0.180$. We set $t_{\text{so}} = t_0 = 1$, $m_x^{(c)} = m_z$, $m_y^{(c)} = 0$, and $m_z^{(c)} = 100$.

Hamiltonian. On the other hand, we introduce a characteristic time t_c such that

$$|m_z^{\text{eff}}(t_c)| = 4t_0, \quad (9)$$

characterizing the critical time of the dynamical topological phase transition of the postquenched Hamiltonian. Meanwhile, a nontrivial relation $m_z^{\text{eff}}(t_s) = m_z^{\text{eff}}(t_c)$ happens on the topological phase boundaries, giving $t_s = t_c$. We denote this characteristic time on these topological boundaries as t^* , such that

$$n_d(t^*) = n_d^*, \quad (10)$$

which holds a unique value for the system with a fixed spin-orbit coupled strength due to the linear scaling of n_d^* [see Fig. 1(d)]. With these three characteristic timescales t_s , t_c , and t^* , the properties of the equilibrium mean-field Hamiltonian can be completely characterized, where the ground states, the topological phase transition, and the topological phase boundaries are characterized by $\mathcal{H}_{\mathbf{k}}(t_s)$, $\mathcal{H}_{\mathbf{k}}(t_c)$, and $\mathcal{H}_{\mathbf{k}}(t^*)$, respectively. In Fig. 2, we show that both t_s and t_c emerge in the short-time evolution. Together with t^* in Fig. 5(b), we clearly observe that the relative timescales behave differently for the different equilibrium mean-field phases. This result provides a basic idea to establish the topological characterization and to detect the mean-field phase diagram. We shall theoretically calculate the three characteristic times

in Sec. IV, and then we will show how to accurately identify the equilibrium mean-field topological phases via the three timescales in Sec. V.

IV. NONTRIVIAL DYNAMICAL PROPERTIES

In this section, we determine the characteristic times t_s , t_c , and t^* entirely from quantum dynamics, and we provide the analytical results under certain conditions. Also, the nontrivial dynamical properties are uncovered, including the emergence of dynamical self-consistent particle density and the dynamical topological phase transition, and then the scaling properties of the three characteristic times.

A. Dynamical self-consistent particle density and characteristic time t_s

We first figure out how to theoretically determine the characteristic time t_s in the quantum dynamics. A notable fact is that the equilibrium particle density $n_{\uparrow(\downarrow)}$ is self-consistently obtained in the equilibrium mean-field Hamiltonian, and the time-evolved particle density $n_{\uparrow(\downarrow)}(t)$ can be considered as a specific path for updating the mean-field parameters. Hence we introduce another set of time-dependent particle density,

$$\tilde{n}_{\uparrow}(t) = \frac{1}{N} \sum_{\mathbf{k}} |\tilde{\chi}_{\mathbf{k}}(t)|^2, \quad \tilde{n}_{\downarrow}(t) = \frac{1}{N} \sum_{\mathbf{k}} |\tilde{\eta}_{\mathbf{k}}(t)|^2, \quad (11)$$

for the eigenvector $\tilde{\Psi}_{\mathbf{k}}(t) = [\tilde{\chi}_{\mathbf{k}}(t), \tilde{\eta}_{\mathbf{k}}(t)]^T$ of the postquenched Hamiltonian $\mathcal{H}_{\mathbf{k}}(t)$ with negative energy, which can be obtained once we know the instantaneous particle density $n_{\uparrow(\downarrow)}(t)$. Note that $n_{\uparrow(\downarrow)}(t)$ and $\tilde{n}_{\uparrow(\downarrow)}(t)$ are slightly different, where the former is the particle density corresponding to the instantaneous states but the latter is that corresponding to the eigenstates of $\mathcal{H}_{\mathbf{k}}(t)$. We see that $\mathcal{H}_{\mathbf{k}}(t)$ is self-consistent when the two sets of time-dependent particle density coincide, giving the characteristic time

$$t_s \equiv \min\{t | n_{\uparrow(\downarrow)}(t) = \tilde{n}_{\uparrow(\downarrow)}(t)\}, \quad (12)$$

at which there is $n_{\uparrow(\downarrow)} = n_{\uparrow(\downarrow)}(t_s) = \tilde{n}_{\uparrow(\downarrow)}(t_s)$, as we show in Fig. 2. This result determines the dynamical self-consistent particle density $n_{\uparrow(\downarrow)}(t_s)$ and captures the equilibrium self-consistent particle density. Although the measurement of t_s was almost impossible in recent experiments, it clearly characterizes the novel dynamic properties derived from quenching.

In addition, it should be emphasized that here only the time-dependent particle density becomes self-consistent, while the instantaneous wave function does not, which illustrates a subtle difference from the equilibrium mean-field Hamiltonian where both the particle density and the wave function are completely self-consistent (see Appendix C). This implies that the different instantaneous states may lead to the same value of $n_{\uparrow(\downarrow)}(t_s)$ and there may be multiple time points fulfilling the self-consistent condition. We hereby choose the smallest time point as t_s due to the consideration of short-time evolution [see Fig. 2(a)]. Also, a finite t_s shall definitely appear in the short-time evolution, since $n_{\uparrow(\downarrow)}(t)$ increases or decays in this regime and the state gradually reaches a steady state after $t > t_s$.

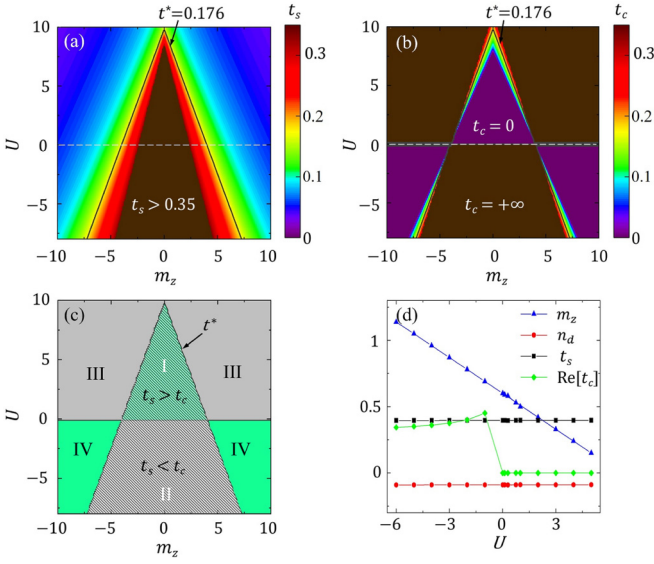


FIG. 3. (a),(b) Analytical results of t_s and t_c , where $t^* = 0.176$ is on the topological boundaries (black solid lines). The dark-brown regions represent $t_s > 0.35$ in (a) and $t_c = +\infty$ in (b), respectively, while the dark-purple regions in (b) give $t_c = 0$. These regions actually correspond to the complex values of t_s and t_c since a large truncation $O(U^3 n_d^3)$ is taken. After reducing the truncation error, t_s gives the real value but t_c still gives a complex value due to no solution. (c) Sign of $t_s - t_c$, where the shaded area is the equilibrium topological phase region. (d) Analytical results of t_s , n_d , and $\text{Re}[t_c]$ at $n_d \approx -0.09$, showing the linear scaling of t_s and n_d . Here we set $t_{so} = t_0 = 1$.

The explicit form of t_s is usually very complex, but we can obtain an analytical result in the short-time evolution for a weak interaction strength or a small $|Un_d|$. After some straightforward calculations, t_s is given by (see Appendix B)

$$t_s \approx \sqrt{\frac{N_1}{N_0 + \sqrt{N_2 + N_3(m_z - n_d U)^2}}} \quad (13)$$

with $N_0 = 12t_{so}^2$, $N_1 = 3(1 \pm 2n_d)$, $N_2 = -28t_{so}^4(\pm 10n_d - 1) - 72t_0^2 t_{so}^2(\pm 2n_d + 1)$, and $N_3 = -28t_{so}^2(\pm 2n_d + 1)$, where \pm corresponds to the sign of m_z . We clearly observe that t_s is associated with n_d and t_{so} . Since the contour lines of n_d have the linear form of interaction strength U and Zeeman coupling m_z , this characteristic time t_s also has a similar linear scaling for a fixed t_{so} , which is presented in Fig. 3(a) and fully matches with the numerical results.

B. Dynamical topological phase transition and characteristic time t_c

We now theoretically determine the characteristic time t_c from the dynamical topological phase transition of postquenched Hamiltonian $\mathcal{H}_k(t)$. As we know, the dynamical topological phase transition is a phase transition in time driven by sharp internal changes in the properties of a quantum many-body state, and it is not driven by an external control parameter [76,77]. Quantum quenching is one way to induce the dynamical phase transitions. When we performing the quench dynamics for this system, the value of $|n_d(t)|$ gen-

erally decays with the time evolution and approaches steady state since the initial state is prepared into a nearly fully polarized state for $t < 0$ and has $n_d(t=0) \approx \pm 0.5$. When the interaction strength satisfies $U > -8t_0$, we find that the time-dependent effective Zeeman coupling $m_z^{\text{eff}}(t)$ only passes through one phase transition point, i.e., $4t_0$ for $m_z > 0$ or $-4t_0$ for $m_z < 0$. Moreover, the corresponding crossover may occur multiple times. Hence $\mathcal{H}_k(t)$ only changes from the trivial (topological) regime at $t = 0$ to the topological (trivial) regime for $t > 0$ when the interaction is repulsive (attractive). To describe the critical time of the dynamical topological phase transition, the characteristic time t_c is naturally defined as

$$t_c \equiv \min\{t | m_z^{\text{eff}}(t) = \pm 4t_0\}. \quad (14)$$

We have $t_c = +\infty$ and 0 ($t_c = 0$ and $+\infty$) in the repulsive (attractive) interaction regime when $|m_z^{\text{eff}}(t)| > 4t_0$ and $|m_z^{\text{eff}}(t)| < 4t_0$, respectively. Here $t_c = +\infty$ of the repulsive interaction means that the topology of $\mathcal{H}_k(t)$ is always trivial in a long evolved time, while a finite t_c implies that its topology is changed from the trivial case with $t < 0$ to the topological case with $t = t_c$.

With the precise definition of t_c , we next numerically show it in Fig. 2, where $m_z^{\text{eff}}(t)$ only passes through the phase transition point $m_z^{\text{eff}}(t_c) = 4t_0$ and decays (increases) for the repulsive (attractive) interaction in the short time region. Note that this feature can be described by the analytical $n_d(t)$ in Appendix B, where we have $m_z^{\text{eff}}(t) \geq 0$ for $Um_z \leq 0$ due to $\dot{m}_z^{\text{eff}}(t) = -Un_d(t)$. In addition, we should choose the minimum timescale in Eq. (14) which is similar to t_s , since the instantaneous state is not self-consistent and there may be multiple time points to satisfy this requirement.

Like Eq. (13), we also obtain an analytical result for t_c in the short-time evolution (see Appendix B) as follows:

$$t_c \approx \sqrt{\frac{P_0 - \sqrt{P_2 - 3P_1(\pm m_z - 4t_0)/U}}{P_1}} \quad (15)$$

with $P_0 = 6t_{so}^2$, $P_1 = 4t_{so}^2(5t_{so}^2 + 19t_0^2)$, and $P_2 = 6t_{so}^2(t_{so}^2 - 19t_0^2)$. Compared with t_s , the characteristic time t_c presents a completely different scaling form in terms of the Zeeman coupling and interaction strength, expect for the topological phase boundaries [see Fig. 3(b)]. This also implies that $t_s = t_c$ happens on these topological boundaries. On the other hand, we observe that finite t_c only appears around the topological phase boundaries. The reason is that $\mathcal{H}_k(t)$ always remains topological or trivial when it is far away from the phase boundaries [this also causes the unchanged dynamical invariant $\nu(t)$ of Eq. (22) in the evolution], as we show in Figs. 5(b) and 5(d).

C. Characteristic time t^* and its linear scaling

We now theoretically determine the characteristic time t^* . Since the postquenched parameters on the topological phase boundaries keep $m_z^{\text{eff}}(t_s) = m_z^{\text{eff}}(t_c)$, a special evolution time can be defined on these topological phase boundaries by

$$t^* \equiv \min\{t | n_d(t) = n_d^*\}, \quad (16)$$

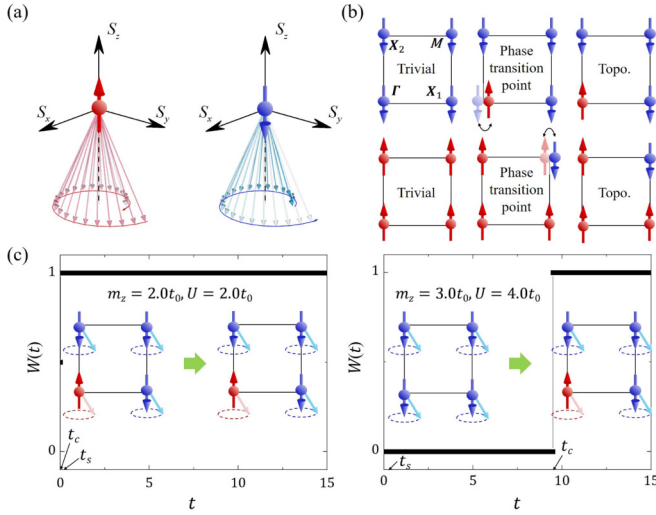


FIG. 4. (a) Schematic diagram for the motion of the nearly fully polarized spin at Dirac points \mathbf{D}_i . The clockwise (counterclockwise) motion of the spin implies the upward (downward) polarization of the Hamiltonian at these points. (b) The polarization directions at Dirac points \mathbf{D}_i determine the topology of the postquenched Hamiltonian. (c) Topological number $W(t)$ for $\mathcal{H}_k(t)$. We have $\text{Ch}_1 = 1$ for the phase with $(m_z, U) = (2, 2)$ due to $t_c = 0 < t_s = 0.165$, while $\text{Ch}_1 = 0$ for the phase with $(m_z, U) = (3, 4)$ due to $t_c = 9.485 > t_s = 0.230$. The insets show the changes of polarization directions at Dirac points \mathbf{D}_i for $\mathcal{H}_k(t)$. Here we set $t_{\text{so}} = t_0 = 1$, $m_x^{(c)} = m_z$, $m_y^{(c)} = 0$, and $m_z^{(c)} = 100$.

which holds the nontrivial relation $t_s = t_c$ [see Figs. 3(a) and 3(b)]. This point can be clearly observed by taking $m_z - Un_d = \pm 4t_0$ in Eqs. (13) and (15), which synchronously gives

$$t^* \approx \sqrt{\frac{B_1}{B_0 + \sqrt{B_2}}}, \quad (17)$$

where $B_0 = 6t_{\text{so}}^2$, $B_1 = 3(1 \pm 2n_d^*)/2$, and $B_2 = -114(1 \pm 2n_d^*)t_0^2 t_{\text{so}}^2 - 6(\pm 10n_d^* - 1)t_{\text{so}}^4$; see Appendix B. For the parameters on the topological boundaries, the gap closing occurs at Dirac points Γ or \mathbf{M} , which is naturally captured by t^* . In addition, it should be noted that t^* is only a timescale corresponding to these topological boundaries, and it is slightly different from the previous t_s and t_c , which can cover all parameters. In particular, we see that the analytical t^* is associated with n_d^* and t_{so} , where n_d^* is usually a constant in the topological phase boundaries and has the linear scaling for the Zeeman coupling and interaction. Hence t^* shall inherit these linear properties and only depend on the spin-orbit coupled strength. As shown in Fig. 3, we have $t^* \propto 1/t_0$ for a strong spin-orbit coupling with $t_{\text{so}} = t_0$, which theoretically gives $t^* = 0.176$ when $t_{\text{so}} = t_0 = 1$, and this agrees with the numerical result $t^* = 0.180$ [see Fig. 5(b)].

V. MEAN-FIELD PHASE DIAGRAM DETERMINED BY TIMESCALES

In this section, we establish the dynamical characterization via the above three timescales. Further, we accurately determine the Chern number by examining the spin dynam-

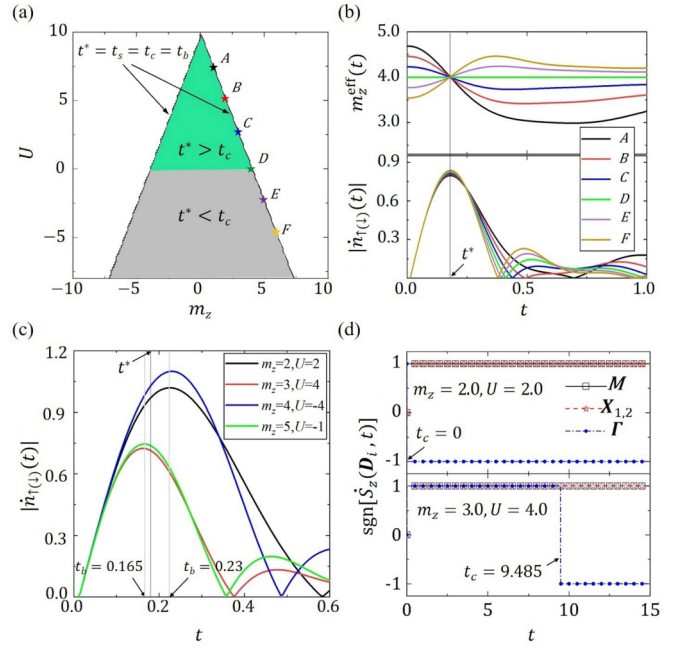


FIG. 5. (a) Mean-field phase diagram determined by the characteristic time t_c and t^* , where the postquenched parameters $A-F$ (stars) are chosen on the topological phase boundaries with $(m_z, U) = (1.0, 7.38)$, $(2.0, 4.92)$, $(3.0, 2.46)$, $(4.0, 0)$, $(5.0, -2.46)$, and $(6.0, -4.92)$. (b) Dynamical evolution of $m_z^{\text{eff}}(t)$ and $|\hat{n}_{\uparrow(\downarrow)}(t)|$ for $A-F$, where $t_c = t^* = 0.180$ (upper) and $t_b = t^* = 0.180$ (lower) with the same scaling. (c) Dynamical evolution of $|\hat{n}_{\uparrow(\downarrow)}(t)|$, where $t_b = 0.165$ for $(m_z, U) = (2.0, 2.0)$ and $(4.0, -4.0)$ while $t_b = 0.230$ for $(m_z, U) = (3.0, 4.0)$ and $(5.0, -1.0)$. (d) Sign of $S_z(\mathbf{D}_i, t)$ at four Dirac points. We have $\text{Ch}_1 = 1$ for the topological phase with $(m_z, U) = (2.0, 2.0)$ due to $t_c = 0 < t^*$ and $\text{Ch}_1 = 0$ for the trivial phase with $(m_z, U) = (3.0, 4.0)$ due to $t_c = 9.485 > t^*$. Here we set $t_{\text{so}} = t_0 = 1$, $m_x^{(c)} = m_z$, $m_y^{(c)} = 0$, and $m_z^{(c)} = 100$.

ics at four Dirac points. In particular, we demonstrate the correctness of the mean-field phase diagram by comparing the dynamical measurement results with the theoretical self-consistent results.

A. Dynamical characterization

In the previous quench dynamics, this interacting system will yield the different timescales in the different postquenched topological phases with the repulsive (attractive) interaction, when $\mathcal{H}_k(t)$ is trivial (topological) at $t = 0$. Specifically, the relations of three timescales are given via the four regimes of Fig. 3(c). Regime I ($U > 0$, topological phase): $t_s > t_c$, $t^* > t_c$, and $t^* < t_s$; regime II ($U < 0$, topological phase): $t_s < t_c$, $t^* < t_c$, and $t^* < t_s$; regime III ($U > 0$, trivial phase): $t_s < t_c$, $t^* < t_c$, and $t^* > t_s$; regime IV ($U < 0$, trivial phase): $t_s > t_c$, $t^* > t_c$, and $t^* > t_s$. Equivalently, the correspondence between the characteristic time and the equilibrium topological properties is given by

$$|\text{Ch}_1| = \begin{cases} 1 & \text{for } \begin{cases} t_s > t^* > t_c, U > 0, \\ t^* < t_s < t_c, U < 0, \end{cases} \\ 0 & \text{for } \begin{cases} t_s < t^* < t_c, U > 0, \\ t^* > t_s > t_c, U < 0. \end{cases} \end{cases} \quad (18)$$

The formula provides a convenient dynamical way to determine the mean-field topological phase by comparing any two characteristic timescales. Moreover, both the numerical results (Fig. 2) and the analytical results [Fig. 3(c)] confirm this, especially for weak interaction U or small $|Un_d|$, as we show in Fig. 3(d). Hence we only need to prepare an initial nearly fully polarized state and perform quenching, and then the mean-field topological phases can be directly determined by comparing any two timescales.

B. Determination of Chern number

For the equilibrium mean-field topological phases of Eq. (18), we further need to accurately determine the Chern number by considering the features of spin dynamics. Specifically, the time-dependent spin evolution of this interacting system is described by the modified Landau-Lifshitz equation [123]

$$\dot{\mathbf{S}}(\mathbf{k}, t) = \mathbf{S}(\mathbf{k}, t) \times 2\mathbf{h}(\mathbf{k}, t) \quad (19)$$

with

$$\begin{aligned} S_x(\mathbf{k}, t) &= [\chi_{\mathbf{k}}(t)\eta_{\mathbf{k}}^*(t) + \chi_{\mathbf{k}}^*(t)\eta_{\mathbf{k}}(t)]/2, \\ S_y(\mathbf{k}, t) &= i[\chi_{\mathbf{k}}(t)\eta_{\mathbf{k}}^*(t) - \chi_{\mathbf{k}}^*(t)\eta_{\mathbf{k}}(t)]/2, \\ S_z(\mathbf{k}, t) &= [|\chi_{\mathbf{k}}(t)|^2 - |\eta_{\mathbf{k}}(t)|^2]/2. \end{aligned} \quad (20)$$

The topological number $W(t)$ of the time-dependent postquenched Hamiltonian $\mathcal{H}_{\mathbf{k}}(t)$ is determined by the spin dynamics of $S_z(\mathbf{D}_i, t)$ at four Dirac points \mathbf{D}_i . The Chern number Ch_1 of the equilibrium mean-field Hamiltonian is then obtained by $W(t_s)$.

We next show two fundamental spin dynamical properties of this interacting system. First, the spin at four Dirac points of the nearly fully polarized initial state will move around the corresponding polarization direction of $\mathcal{H}_{\mathbf{k}}(t)$ after the quantum quench. When the polarization direction is reversed, e.g., from upward to downward, the motion of spin will be reversed at the same time, e.g., from clockwise to counterclockwise; see Fig. 4(a). For this, we can use the motion of spins to determine the polarization direction of $\mathcal{H}_{\mathbf{k}}(t)$ at Dirac points. Second, since the polarization direction is associated with the parity eigenvalue of the occupied eigenstate, the topology of $\mathcal{H}_{\mathbf{k}}(t)$ can be identified from the polarization directions at four Dirac points [68], as shown in Fig. 4(b). For instance, the polarization directions at four Dirac points are the same for an initial trivial Hamiltonian $\mathcal{H}_{\mathbf{k}}(t)$. Once it enters the topological regime, the motion of spin at the Γ or \mathbf{M} point will be reversed, manifesting the change of the corresponding polarization direction. This signal can be captured by $\text{sgn}[\dot{S}_z(\mathbf{D}_i, t)]$, as shown in Fig. 5(d). Correspondingly, the topological transition time of the motion of spin just gives the characteristic time t_c .

With the above two fundamental properties, we can define the time-dependent dynamical invariant for $\mathcal{H}_{\mathbf{k}}(t)$ as

$$(-1)^{\nu(t)} = \prod_i \text{sgn}[\dot{S}_z(\mathbf{D}_i, t)], \quad (21)$$

with $\nu(t) = 1$ for the topological regime $|m_z^{\text{eff}}(t)| < 4t_0$ and $\nu(t) = 0$ for the trivial regime $|m_z^{\text{eff}}(t)| > 4t_0$, respectively. The topological transition time of this dynamical invariant

gives the characteristic time t_c as follows:

$$t_c = \begin{cases} 0 & \text{for } \nu(t) = 1 (0), U > 0 (U < 0), \\ \text{finite} & \text{for } \nu(t) = 1 \leftrightarrow \nu(t) = 0, \\ +\infty & \text{for } \nu(t) = 0 (1), U > 0 (U < 0). \end{cases} \quad (22)$$

Here a finite t_c is captured by the critical time of changing of $\nu(t)$ from 1 (0) to 0 (1) [see Figs. 3(b) and 5(d)], while the unchanged $\nu(t)$ in a long-time evolution hosts $t_c = 0$ or $+\infty$. Now the topological number $W(t)$ of $\mathcal{H}_{\mathbf{k}}(t)$ and the Chern number of $\mathcal{H}_{\mathbf{k}}^{\text{MF}}$ can be exactly given by

$$W(t) = \frac{\nu(t)}{2} \sum_i \text{sgn}[\dot{S}_z(\mathbf{D}_i, t)], \quad \text{Ch}_1 = W(t_s). \quad (23)$$

As an example, the numerical results in Fig. 4(c) show the nontrivial topology with $\text{Ch}_1 = 1$ and the trivial topology with $\text{Ch}_1 = 0$ for the postquenched system with $(m_z, U) = (2, 2)$ and $(3, 4)$, respectively. On the other hand, since there is only one topological phase transition point in the dynamical evolution, $W(t)$ has the same value at t_s with t^* . Hence we also have

$$\text{Ch}_1 \simeq W(t^*). \quad (24)$$

It should be emphasized that either Eq. (23) or Eq. (24) can facilitate the determination of Chern number of the equilibrium mean-field topological phases for the postquenched system. In the following, we take Eq. (24) in the experiment for identifying the Chern number due to the easy measurement of t^* .

VI. EXPERIMENTAL DETECTION

Based on the above topological characterization, we next propose a feasible experimental scheme to detect the mean-field topological phase diagram by directly measuring the two characteristic timescales t_c and t^* , without any prior postquenched parameters such as m_z and U . Note that the measurement of t_s is almost impossible in the recent experiment, since it does not have any measurable quantities but only corresponds to the self-consistency of the postquenched Hamiltonian.

In a realistic experiment, identifying the timescale of t_c requires us to measure the spin dynamics of $S_z(\mathbf{D}_i, t)$ at four Dirac points \mathbf{D}_i in a short-time evolution and calculate their changing with the evolved time, i.e., $\dot{S}_z(\mathbf{D}_i, t)$. t_c is then captured by the topological transition time of $\nu(t)$ based on Eq. (22). On the other hand, we need to measure the time-dependent particle density $n_{\uparrow(\downarrow)}(t)$ and calculate the fastest changing of $n_{\uparrow(\downarrow)}(t)$ with the evolved time and identify the timescale of t^* by an auxiliary time

$$t_b \equiv \min\{t | \dot{n}_{\uparrow(\downarrow)}(t) = 0\}. \quad (25)$$

We see that t_b characterizes the evolution of the changes of $n_{\uparrow(\downarrow)}(t)$ the fastest, i.e., $|\dot{n}_{\uparrow(\downarrow)}(t)|$ is maximal. In particular, $t_b = t^*$ occurs on the topological phase boundaries, although it is larger (smaller) than t^* in the topological (trivial) regime [see Fig. 5(c)]. This point can be clearly observed by an

analytical result from Eq. (25), i.e.,

$$t^* \approx \sqrt{\frac{3}{Q_0 + Q_1}} \quad (26)$$

with $Q_0 = \sqrt{-135t_0^2 + 606t_0^2t_{so}^2 + 57t_{so}^4}$ and $Q_1 = 57t_0^2 + 15t_{so}^2$. This formula is consistent with Eq. (17). Also, we have $t^* \approx 0.178$ for $t_0 = t_{so} = 1$, which is approximately equal to $t^* = 0.176$ in Eq. (17).

With the above observation, the mean-field topological phase diagram can be obtained by only comparing both timescales of t_c and t^* ; see Fig. 5(a). Considering that the 2D QAH model was realized in cold atoms [60], and the interaction can be tuned in experiment [43], we hereby provide the following four concrete steps to detect the equilibrium mean-field topological phases for the cold-atom experiment:

Step I: Preparing the nearly fully polarized initial state for the system with $U = 0$, which can be reached by tuning, say, the magnetic field for ultracold atoms. By further varying the two-photon detuning via the bias magnetic field to produce a large m_z , together with turning off one of the electro-optic modulators to generate the small constant magnetization $m_x\sigma_x$ or $m_y\sigma_y$ [124], the nearly fully polarized state is now obtained.

Step II: Performing quench dynamics for this system with $U = 0$. We suddenly change the magnetic field to produce a finite $m_z = \pm 4t_0$ and turn off both of the electro-optic modulators to generate $m_{x(y)} = 0$, which drives the system to evolve over time. Then, we measure the time-dependent particle density $n_{\uparrow(\downarrow)}(t)$. The timescale of t^* is obtained by the fastest changing time point of $n_{\uparrow(\downarrow)}(t)$. Note that this t^* has the linear scaling on the mean-field topological phase boundaries [see Fig. 3(c)], and it is independent of U . Hence t^* can be directly employed to the cases of $U \neq 0$.

Step III: Preparing the nearly fully polarized initial state for the system with $U \neq 0$. This step is similar to Step I. Here U can be an unknown value.

Step IV: Performing quench dynamics for this system with the nonzero U . For this we suddenly tune the system to a regime with an unknown suitable m_z and turn off both of the electro-optic modulators to generate $m_{x(y)} = 0$. Simultaneously, we measure the evolution of $S_z(\mathbf{D}_i, t)$ at four Dirac points and obtain their changing with the evolved time, i.e., $S_z(\mathbf{D}_i, t)$. Then t_c is captured by the topological transition time of $\nu(t)$ based on Eq. (22). Finally, the mean-field topological phases are identified by comparing t^* in Step II and t_c in Step IV, where the Chern number is given by $\text{Ch}_1 \simeq W(t^*)$; see Eq. (24).

With this scheme, the mean-field phase diagram of the interacting Chern insulator can be completely determined, which paves the way for experimentally study of topological phases in interacting systems, and the discovery of new phases.

VII. CONCLUSION AND DISCUSSION

In conclusion, we have studied the 2D QAH model with a weak-to-intermediate Hubbard interaction by performing quantum quenches. A nonequilibrium detection scheme for the mean-field topological phase diagram is proposed by observing three characteristic times t_s , t_c , and t^* that emerged

in dynamics. We reveal three nontrivial dynamical properties: (i) t_s and t_c capture the emergence of dynamical self-consistent particle density and dynamical topological phase transition for the time-dependent postquenched Hamiltonian, respectively, while t^* gives a linear scaling time on the topological phase boundaries. (ii) After quenching the Zeeman coupling from the trivial regime to the topological regime, $t_s > t^* > t_c$ ($t^* < t_s < t_c$) is observed for the repulsive (attractive) interaction. (iii) The Chern number of postquenched mean-field topological phase can be determined by comparing any two timescales. These results provide a feasible scheme to detect the mean-field topological phases of an interacting Chern insulator, and they may be applied to the quantum simulation experiments.

The present dynamical scheme can be applied to the Chern insulator with the weak-to-intermediate interaction. On the other hand, when the general strong interactions are considered, the system may host more abundant magnetic phases [115–117]. Generalizing these dynamical properties to the related studies and further identifying the rich topological phases would be interesting and worthwhile work in the future.

ACKNOWLEDGMENTS

We acknowledge the valuable discussions with Sen Niu and Ting Fung Jeffrey Poon. This work was supported by National Natural Science Foundation of China (Grants No. 11825401 and No. 11921005), the National Key R&D Program of China (Project No. 2021YFA1400900), Strategic Priority Research Program of the Chinese Academy of Science (Grant No. XDB28000000), and by the Innovation Program for Quantum Science and Technology (Grant No. 2021ZD0302000). L.Z. also acknowledges support from the startup grant of the Huazhong University of Science and Technology (Grant No. 3004012191). L.Z. also acknowledges support from Agencia Estatal de Investigación (the R&D project CEX2019-000910-S, funded by MCIN/AEI/10.13039/501100011033, Plan National FIDEUA PID2019-106901GB-I00, FPI), Fundació Privada Cellex, Fundació Mir-Puig, Generalitat de Catalunya (AGAUR Grant No. 2017 SGR 1341, CERCA program), EU Horizon 2020 FET-OPEN OPTologic (Grant No. 899794), and Junior Leaders fellowship LCF/BQ/PI19/11690013 of “La Caixa” Foundation (ID100010434).

APPENDIX A: EQUILIBRIUM ANALYTICAL RESULTS

In the presence of the nonzero interaction, the equilibrium mean-field Hamiltonian $\mathcal{H}_k^{\text{MF}}$ self-consistently gives the difference of density for spin-up and spin-down particles as $n_d \equiv (n_{\uparrow} - n_{\downarrow})/2$ under the mean-field theory. Here we explicitly show

$$n_d = \frac{1}{N} \sum_{\mathbf{k}} \frac{-h_{z,\mathbf{k}} + Un_d}{2\sqrt{h_{x,\mathbf{k}}^2 + h_{y,\mathbf{k}}^2 + (h_{z,\mathbf{k}} - Un_d)^2}}. \quad (\text{A1})$$

Considering that $|n_d| < 0.5$ is a small value due to the total particle density being conserved, i.e., $n_{\uparrow} + n_{\downarrow} = 1$, we use Taylor series at $n_d = 0$ for the right-hand term of Eq. (A1), which gives $A_0 + A_1Un_d + A_2U^2n_d^2 + \dots + A_lU^l n_d^l$,

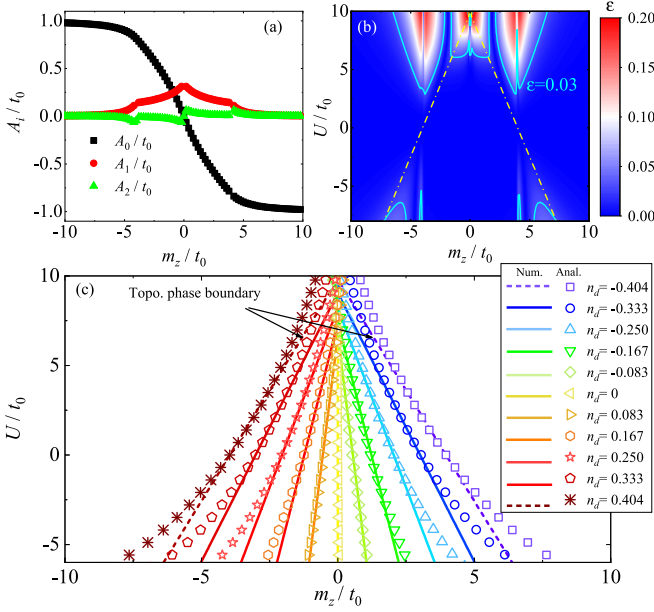


FIG. 6. (a) Analytical coefficients A_0 , A_1 , and A_2 . (b) Absolute error ε between the analytical results and the numerical results for n_d . (c) Analytical results of n_d corresponding to the numerical results shown in Fig. 1(d), giving the linear scaling. Here we set $t_{so} = t_0$.

with $(l+1)$ th-order truncation $O(U^{l+1}n_d^{l+1})$. Here the coefficients $A_{i=0,1,\dots,l}$ satisfy $\partial A_0/\partial h_{z,\mathbf{k}} = -A_1$, $\partial A_1/\partial h_{z,\mathbf{k}} = -2A_2$, $\partial A_2/\partial h_{z,\mathbf{k}} = -3A_3, \dots$. In principle, we can obtain n_d by solving $n_d \approx A_0 + A_1 U n_d + A_2 U^2 n_d^2 + \dots + A_l U^l n_d^l$. The analytical n_d for $l=2$ at a weak interaction or a small Zeeman coupling is approximately given by

$$n_d \approx \frac{2 - A_1 U - \sqrt{(2 - A_1 U)^2 - 4A_0 A_2 U^2}}{2A_2 U^2}, \quad (\text{A2})$$

with $A_0 = \frac{1}{N} \sum_{\mathbf{k}} \frac{-h_{z,\mathbf{k}}}{e_{\mathbf{k}}}$, $A_1 = \frac{1}{N} \sum_{\mathbf{k}} \frac{h_{x,\mathbf{k}}^2 + h_{y,\mathbf{k}}^2}{e_{\mathbf{k}}^3}$, and $A_2 = \frac{1}{N} \sum_{\mathbf{k}} \frac{3(h_{x,\mathbf{k}}^2 + h_{y,\mathbf{k}}^2)h_z}{2e_{\mathbf{k}}^5}$. Equation (A2) shows the scaling property of n_d for m_z and U .

In addition, we observe that A_i can converge to zero for an increased i ; see Fig. 6(a). For a third-order truncation $O(U^3 n_d^3)$ in Eq. (A2), the absolute error ε between analytical and numerical results presents $\varepsilon < 0.03$ for $|U| < 6t_0$, which implies that the precision of third-order truncation is enough. Therefore, Eq. (A2) is applicable to the almost completely topological phase region and all the topological phase boundaries and a large trivial regions, as shown in Fig. 6(b). Also, the analytical results are almost confirmed with the numerical results for both a weak interaction or a small m_z , as shown in Fig. 6(c).

APPENDIX B: NONEQUILIBRIUM ANALYTICAL RESULTS

Considering that the spin of initial state is nearly fully polarized to downward or upward, we can take $[\chi_{\mathbf{k}}(0), \eta_{\mathbf{k}}(0)]^T \approx (0, 1)^T$ or $[\chi_{\mathbf{k}}(0), \eta_{\mathbf{k}}(0)]^T \approx (1, 0)^T$, which corresponds to the postquenched $m_z > 0$ or $m_z < 0$. Further, the change of $n_d(t)$ is small during a short-time

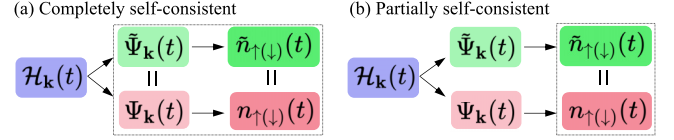


FIG. 7. Flowcharts for the self-consistent calculation of particle density. (a) Completely self-consistent. (b) Partially self-consistent.

evolution, and it can be regarded as a constant in a very short time. By solving Eq. (4), we can obtain $n_d(t) \approx n_{d,t}$, which is given by

$$n_{d,t} = \pm \frac{1}{N} \sum_{\mathbf{k}} \frac{-e_{\mathbf{k},t}^2 + (h_{x,\mathbf{k}}^2 + h_{y,\mathbf{k}}^2)(1 - \cos 2te_{\mathbf{k},t})}{2e_{\mathbf{k},t}^2}, \quad (\text{B1})$$

where $e_{\mathbf{k},t} = \sqrt{h_{x,\mathbf{k}}^2 + h_{y,\mathbf{k}}^2 + (h_{z,\mathbf{k}} - n_{d,t}U)^2}$, and \pm corresponds to the sign of the postquenched m_z . Similarly, we use Taylor series at $n_{d,t} = 0$ for the right-hand term of Eq. (B1), which gives $D_0 + D_1 U n_{d,t} + D_2 U^2 n_{d,t}^2 + \dots + D_l U^l n_{d,t}^l$ with $(l+1)$ th-order truncation $O(U^{l+1}n_{d,t}^{l+1})$.

We next take the third-order truncation $O(U^3 n_{d,t}^3)$ to approximately obtain $n_{d,t}$ as follows:

$$n_{d,t} \approx \frac{2 - D_1 U - \sqrt{(2 - D_1 U)^2 - 4D_0 D_2 U^2}}{2D_2 U^2} \quad (\text{B2})$$

with $D_0 = \pm 8t_{so}^2 t^2 - [\pm 1 \pm 8t_{so}^2(m_z^2 + 3t_0^2 + 5t_{so}^2)t^4/3]$, $D_1 = \pm 16m_z t_{so}^2 t^4/3$, and $D_2 = -(\pm 8t_{so}^2 t^4/3)$. Note that here we have used Taylor series at $t=0$ for $D_{0,1,2}$ and have taken sixth-order truncation $O(t^6)$ for t . Then this approximate $n_{d,t}$ is only suitable for a short-time evolution or a small value of $|U n_{d,t}|$. Finally, we explicitly give t_s , t_c , t^* , and t_b by solving the equations of $n_{d,t} = n_d$, $m_z - U n_{d,t} = \pm 4t_0$, $n_d(t) = n_d^*$, and $\dot{n}_{d,t} = 0$, respectively, where the theoretical results are shown in Eqs. (13), (15), (17), and (26).

APPENDIX C: DYNAMICAL SELF-CONSISTENT PROCESSES OF PARTICLE DENSITY

There are two cases of the dynamical self-consistent processes to obtain the self-consistent particle density $\tilde{n}_{\uparrow(\downarrow)}(t)$. The first one is a completely self-consistent process, i.e., both the wave function and the particle density are self-consistent, as is shown in Fig. 7(a). By diagonalizing the time-dependent Hamiltonian $\mathcal{H}_{\mathbf{k}}(t)$ and obtaining its eigenvector, $\tilde{\Psi}_{\mathbf{k}}(t) = [\tilde{\chi}_{\mathbf{k}}(t), \tilde{\eta}_{\mathbf{k}}(t)]^T$ with negative energy. Next the instantaneous wave function $\Psi_{\mathbf{k}}(t)$ should equal $\tilde{\Psi}_{\mathbf{k}}(t)$ at each momentum \mathbf{k} , i.e., $\Psi_{\mathbf{k}}(t) = \tilde{\Psi}_{\mathbf{k}}(t)$. It is clear that the self-consistent wave function directly gives $n_{\uparrow(\downarrow)}(t) = \tilde{n}_{\uparrow(\downarrow)}(t)$ from Eqs. (5) and (11). In particular, we emphasize that this system shall reach a dynamical balance, and both m_z^{eff} and $n_{\uparrow(\downarrow)}(t)$ do not evolve with time when $\Psi_{\mathbf{k}}(t)$ becomes the eigenvector of $\mathcal{H}_{\mathbf{k}}(t)$.

The second one is a partially self-consistent process, i.e., only the particle density is self-consistent, as is shown in Fig. 7(b). After obtaining the eigenvector $\tilde{\Psi}_{\mathbf{k}}(t) = [\tilde{\chi}_{\mathbf{k}}(t), \tilde{\eta}_{\mathbf{k}}(t)]^T$ with negative energy of $\mathcal{H}_{\mathbf{k}}(t)$, the difference from the above process is that we directly take $n_{\uparrow(\downarrow)}(t)$ equal to $\tilde{n}_{\uparrow(\downarrow)}(t)$, and we do not care about the instantaneous states. It is clear that the self-consistent particle density is also given by $n_{\uparrow(\downarrow)}(t) = \tilde{n}_{\uparrow(\downarrow)}(t)$, but now the wave function is not self-consistent, i.e., $\Psi_{\mathbf{k}}(t) \neq \tilde{\Psi}_{\mathbf{k}}(t)$. Physically, the particle density is associated with the summation of the wave function at all

\mathbf{k} , which implies that the wave function of each \mathbf{k} may not be self-consistent but the summation for all \mathbf{k} can be self-consistent.

Both processes can provide the self-consistent particle density of postquenched Hamiltonian $\mathcal{H}_{\mathbf{k}}(t)$, but it is difficult to realize the completely self-consistent particle density in a long-term evolution. The particle density is easily obtained in a short-time evolution, which is also more helpful in capturing the nontrivial dynamics.

-
- [1] K. v. Klitzing, G. Dorda, and M. Pepper, New Method for High-Accuracy Determination of the Fine-Structure Constant Based on Quantized Hall Resistance, *Phys. Rev. Lett.* **45**, 494 (1980).
- [2] D. C. Tsui, H. L. Stormer, and A. C. Gossard, Two-Dimensional Magnetotransport in the Extreme Quantum Limit, *Phys. Rev. Lett.* **48**, 1559 (1982).
- [3] M. Z. Hasan and C. L. Kane, Colloquium: topological insulators, *Rev. Mod. Phys.* **82**, 3045 (2010).
- [4] X.-G. Wen, Colloquium: Zoo of quantum-topological phases of matter, *Rev. Mod. Phys.* **89**, 041004 (2017).
- [5] J. M. Kosterlitz, Nobel lecture: topological defects and phase transitions, *Rev. Mod. Phys.* **89**, 040501 (2017).
- [6] X.-G. Wen, Topological orders in rigid states, *Int. J. Mod. Phys. B* **04**, 239 (1990).
- [7] X.-L. Qi and S.-C. Zhang, Topological insulators and superconductors, *Rev. Mod. Phys.* **83**, 1057 (2011).
- [8] L. Fu, C. L. Kane, and E. J. Mele, Topological Insulators in Three Dimensions, *Phys. Rev. Lett.* **98**, 106803 (2007).
- [9] L. Fu and C. L. Kane, Topological insulators with inversion symmetry, *Phys. Rev. B* **76**, 045302 (2007).
- [10] L. Fu, Topological Crystalline Insulators, *Phys. Rev. Lett.* **106**, 106802 (2011).
- [11] C.-Z. Chang, J. Zhang, X. Feng, J. Shen, Z. Zhang, M. Guo, K. Li, Y. Ou, P. Wei, L.-L. Wang, Z.-Q. Ji, Y. Feng, S. Ji, X. Chen, J. Jia, X. Dai, Z. Fang, S.-C. Zhang, K. He, Y. Wang *et al.*, Experimental observation of the quantum anomalous Hall effect in a magnetic topological insulator, *Science* **340**, 167 (2013).
- [12] A. A. Burkov and L. Balents, Weyl Semimetal in a Topological Insulator Multilayer, *Phys. Rev. Lett.* **107**, 127205 (2011).
- [13] S. M. Young, S. Zaheer, J. C. Y. Teo, C. L. Kane, E. J. Mele, and A. M. Rappe, Dirac Semimetal in Three Dimensions, *Phys. Rev. Lett.* **108**, 140405 (2012).
- [14] S.-Y. Xu, I. Belopolski, N. Alidoust, M. Neupane, G. Bian, C. Zhang, R. Sankar, G. Chang, Z. Yuan, C.-C. Lee, S.-M. Huang, H. Zheng, J. Ma, D. S. Sanchez, B. Wang, A. Bansil, F. Chou, P. P. Shibayev, H. Lin, S. Jia *et al.*, Discovery of a Weyl fermion semimetal and topological Fermi arcs, *Science* **349**, 613 (2015).
- [15] B. Q. Lv, H. M. Weng, B. B. Fu, X. P. Wang, H. Miao, J. Ma, P. Richard, X. C. Huang, L. X. Zhao, G. F. Chen, Z. Fang, X. Dai, T. Qian, and H. Ding, Experimental Discovery of Weyl Semimetal TaAs, *Phys. Rev. X* **5**, 031013 (2015).
- [16] X.-L. Qi, T. L. Hughes, S. Raghu, and S.-C. Zhang, Time-Reversal-Invariant Topological Superconductors and Superfluids in Two and Three Dimensions, *Phys. Rev. Lett.* **102**, 187001 (2009).
- [17] B. A. Bernevig and T. L. Hughes, *Topological Insulators and Topological Superconductors* (Princeton University Press, Princeton, NJ, 2013).
- [18] Y. Ando and L. Fu, Topological crystalline insulators and topological superconductors: From concepts to materials, *Annu. Rev. Condens. Matter Phys.* **6**, 361 (2015).
- [19] M. Sato and Y. Ando, Topological superconductors: a review, *Rep. Prog. Phys.* **80**, 076501 (2017).
- [20] P. Zhang, K. Yaji, T. Hashimoto, Y. Ota, T. Kondo, K. Okazaki, Z. Wang, J. Wen, G. Gu, H. Ding, and S. Shin, Observation of topological superconductivity on the surface of an iron-based superconductor, *Science* **360**, 182 (2018).
- [21] Z. Wang, X.-L. Qi, and S.-C. Zhang, Topological Order Parameters for Interacting Topological Insulators, *Phys. Rev. Lett.* **105**, 256803 (2010).
- [22] D. Pesin and L. Balents, Mott physics and band topology in materials with strong spin-orbit interaction, *Nat. Phys.* **6**, 376 (2010).
- [23] D.-H. Lee, Effects of Interaction on Quantum Spin Hall Insulators, *Phys. Rev. Lett.* **107**, 166806 (2011).
- [24] E. V. Castro, A. G. Grushin, B. Valenzuela, M. A. H. Vozmediano, A. Cortijo, and F. de Juan, Topological Fermi Liquids from Coulomb Interactions in the Doped Honeycomb Lattice, *Phys. Rev. Lett.* **107**, 106402 (2011).
- [25] M. A. N. Araújo, E. V. Castro, and P. D. Sacramento, Change of an insulator's topological properties by a Hubbard interaction, *Phys. Rev. B* **87**, 085109 (2013).
- [26] H. Yao and S. Ryu, Interaction effect on topological classification of superconductors in two dimensions, *Phys. Rev. B* **88**, 064507 (2013).
- [27] M. Messer, R. Desbuquois, T. Uehlinger, G. Jotzu, S. Huber, D. Greif, and T. Esslinger, Exploring Competing Density Order in the Ionic Hubbard Model with Ultracold Fermions, *Phys. Rev. Lett.* **115**, 115303 (2015).
- [28] E. M. Spanton, A. A. Zibrov, H. Zhou, T. Taniguchi, K. Watanabe, M. P. Zaletel, and A. F. Young, Observation of fractional chern insulators in a van der waals heterostructure, *Science* **360**, 62 (2018).
- [29] S. Rachel, Interacting topological insulators: a review, *Rep. Prog. Phys.* **81**, 116501 (2018).
- [30] O. Viyuela, L. Fu, and M. A. Martin-Delgado, Chiral Topological Superconductors Enhanced by Long-Range Interactions, *Phys. Rev. Lett.* **120**, 017001 (2018).

- [31] B. Andrews and A. Soluyanov, Fractional quantum hall states for moiré superstructures in the hofstadter regime, *Phys. Rev. B* **101**, 235312 (2020).
- [32] A. Mook, K. Plekhanov, J. Klinovaja, and D. Loss, Interaction-Stabilized Topological Magnon Insulator in Ferromagnets, *Phys. Rev. X* **11**, 021061 (2021).
- [33] S. Raghu, X.-L. Qi, C. Honerkamp, and S.-C. Zhang, Topological Mott Insulators, *Phys. Rev. Lett.* **100**, 156401 (2008).
- [34] S. Rachel and K. Le Hur, Topological insulators and Mott physics from the Hubbard interaction, *Phys. Rev. B* **82**, 075106 (2010).
- [35] T. I. Vanhala, T. Siro, L. Liang, M. Troyer, A. Harju, and P. Törmä, Topological Phase Transitions in the Repulsively Interacting Haldane-Hubbard Model, *Phys. Rev. Lett.* **116**, 225305 (2016).
- [36] X.-L. Qi, Y.-S. Wu, and S.-C. Zhang, Topological quantization of the spin hall effect in two-dimensional paramagnetic semiconductors, *Phys. Rev. B* **74**, 085308 (2006).
- [37] X.-L. Qi, T. L. Hughes, and S.-C. Zhang, Chiral topological superconductor from the quantum Hall state, *Phys. Rev. B* **82**, 184516 (2010).
- [38] X.-J. Liu, K. T. Law, and T. K. Ng, Realization of 2D Spin-Orbit Interaction and Exotic Topological Orders in Cold Atoms, *Phys. Rev. Lett.* **112**, 086401 (2014).
- [39] T. F. J. Poon and X.-J. Liu, From a semimetal to a chiral Fulde-Ferrell superfluid, *Phys. Rev. B* **97**, 020501(R) (2018).
- [40] W. Hofstetter and T. Qin, Quantum simulation of strongly correlated condensed matter systems, *J. Phys. B* **51**, 082001 (2018).
- [41] B. Fauseweh and J.-X. Zhu, Digital quantum simulation of non-equilibrium quantum many-body systems, *Quant. Inf. Proc.* **20**, 138 (2021).
- [42] C. Monroe, W. C. Campbell, L.-M. Duan, Z.-X. Gong, A. V. Gorshkov, P. W. Hess, R. Islam, K. Kim, N. M. Linke, G. Pagano, P. Richerme, C. Senko, and N. Y. Yao, Programmable quantum simulations of spin systems with trapped ions, *Rev. Mod. Phys.* **93**, 025001 (2021).
- [43] I. Bloch, J. Dalibard, and W. Zwerger, Many-body physics with ultracold gases, *Rev. Mod. Phys.* **80**, 885 (2008).
- [44] T. Langen, R. Geiger, and J. Schmiedmayer, Ultracold atoms out of equilibrium, *Annu. Rev. Condens. Matter Phys.* **6**, 201 (2015).
- [45] C. Gross and I. Bloch, Quantum simulations with ultracold atoms in optical lattices, *Science* **357**, 995 (2017).
- [46] M. Schreiber, S. S. Hodgman, P. Bordia, H. P. Lüschen, M. H. Fischer, R. Vosk, E. Altman, U. Schneider, and I. Bloch, Observation of many-body localization of interacting fermions in a quasirandom optical lattice, *Science* **349**, 842 (2015).
- [47] J. Smith, A. Lee, P. Richerme, B. Neyenhuis, P. W. Hess, P. Hauke, M. Heyl, D. A. Huse, and C. Monroe, Many-body localization in a quantum simulator with programmable random disorder, *Nat. Phys.* **12**, 907 (2016).
- [48] P. Bordia, H. P. Lüschen, S. S. Hodgman, M. Schreiber, I. Bloch, and U. Schneider, Coupling Identical One-dimensional Many-Body Localized Systems, *Phys. Rev. Lett.* **116**, 140401 (2016).
- [49] J.-y. Choi, S. Hild, J. Zeiher, P. Schauß, A. Rubio-Abadal, T. Yefsah, V. Khemani, D. A. Huse, I. Bloch, and C. Gross, Exploring the many-body localization transition in two dimensions, *Science* **352**, 1547 (2016).
- [50] V. V. Ramasesh, E. Flurin, M. Rudner, I. Siddiqi, and N. Y. Yao, Direct Probe of Topological Invariants Using Bloch Oscillating Quantum Walks, *Phys. Rev. Lett.* **118**, 130501 (2017).
- [51] Z. Jiang, K. J. Sung, K. Kechedzhi, V. N. Smelyanskiy, and S. Boixo, Quantum Algorithms to Simulate Many-Body Physics of Correlated Fermions, *Phys. Rev. Appl.* **9**, 044036 (2018).
- [52] Z. Yan, Y.-R. Zhang, M. Gong, Y. Wu, Y. Zheng, S. Li, C. Wang, F. Liang, J. Lin, Y. Xu, C. Guo, L. Sun, C.-Z. Peng, K. Xia, H. Deng, H. Rong, J. Q. You, F. Nori, H. Fan, X. Zhu *et al.*, Strongly correlated quantum walks with a 12-qubit superconducting processor, *Science* **364**, 753 (2019).
- [53] W. P. Su, J. R. Schrieffer, and A. J. Heeger, Soliton excitations in polyacetylene, *Phys. Rev. B* **22**, 2099 (1980).
- [54] M. Atala, M. Aidelsburger, J. T. Barreiro, D. Abanin, T. Kitagawa, E. Demler, and I. Bloch, Direct measurement of the Zak phase in topological Bloch bands, *Nat. Phys.* **9**, 795 (2013).
- [55] X.-J. Liu, Z.-X. Liu, and M. Cheng, Manipulating Topological Edge Spins in a One-Dimensional Optical Lattice, *Phys. Rev. Lett.* **110**, 076401 (2013).
- [56] B. Song, L. Zhang, C. He, T. F. J. Poon, E. Hājijev, S. Zhang, X.-J. Liu, and G.-B. Jo, Observation of symmetry-protected topological band with ultracold fermions, *Sci. Adv.* **4**, ea04748 (2018).
- [57] F. D. M. Haldane, Continuum dynamics of the 1-D Heisenberg antiferromagnet: Identification with the O(3) nonlinear sigma model, *Phys. Lett. A* **93**, 464 (1983).
- [58] S. de Léséleuc, V. Lienhard, P. Scholl, D. Barredo, S. Weber, N. Lang, H. P. Büchler, T. Lahaye, and A. Browaeys, Observation of a symmetry-protected topological phase of interacting bosons with Rydberg atoms, *Science* **365**, 775 (2019).
- [59] G. Jotzu, M. Messer, R. Desbuquois, M. Lebrat, T. Uehlinger, D. Greif, and T. Esslinger, Experimental realization of the topological Haldane model with ultracold fermions, *Nature* **515**, 237 (2014).
- [60] Z. Wu, L. Zhang, W. Sun, X.-T. Xu, B.-Z. Wang, S.-C. Ji, Y. Deng, S. Chen, X.-J. Liu, and J.-W. Pan, Realization of two-dimensional spin-orbit coupling for Bose-Einstein condensates, *Science* **354**, 83 (2016).
- [61] W. Sun, B.-Z. Wang, X.-T. Xu, C.-R. Yi, L. Zhang, Z. Wu, Y. Deng, X.-J. Liu, S. Chen, and J.-W. Pan, Highly Controllable and Robust 2D Spin-Orbit Coupling for Quantum Gases, *Phys. Rev. Lett.* **121**, 150401 (2018).
- [62] M.-C. Liang, Y.-D. Wei, L. Zhang, X.-J. Wang, H. Zhang, W.-W. Wang, W. Qi, X.-J. Liu, and X. Zhang, Realization of Qi-Wu-Zhang model in spin-orbit-coupled ultracold fermions, *Phys. Rev. Res.* **5**, L012006 (2023).
- [63] W.-Y. He, S. Zhang, and K. T. Law, Realization and detection of Weyl semimetals and the chiral anomaly in cold atomic systems, *Phys. Rev. A* **94**, 013606 (2016).
- [64] B.-Z. Wang, Y.-H. Lu, W. Sun, S. Chen, Y. Deng, and X.-J. Liu, Dirac-, rashba-, and weyl-type spin-orbit couplings: Toward experimental realization in ultracold atoms, *Phys. Rev. A* **97**, 011605(R) (2018).
- [65] Y.-H. Lu, B.-Z. Wang, and X.-J. Liu, Ideal weyl semimetal with 3d spin-orbit coupled ultracold quantum gas, *Sci. Bull.* **65**, 2080 (2020).

- [66] Z.-Y. Wang, X.-C. Cheng, B.-Z. Wang, J.-Y. Zhang, Y.-H. Lu, C.-R. Yi, S. Niu, Y. Deng, X.-J. Liu, S. Chen, and J.-W. Pan, Realization of an ideal Weyl semimetal band in a quantum gas with 3D spin-orbit coupling, *Science* **372**, 271 (2021).
- [67] X. Li and W. V. Liu, Weyl semimetal made ideal with a crystal of raman light and atoms, *Sci. Bull.* **66**, 1253 (2021).
- [68] X.-J. Liu, K.-T. Law, T.-K. Ng, and P. A. Lee, Detecting Topological Phases in Cold Atoms, *Phys. Rev. Lett.* **111**, 120402 (2013).
- [69] M. Hafezi, Measuring Topological Invariants in Photonic Systems, *Phys. Rev. Lett.* **112**, 210405 (2014).
- [70] J. Wu, J. Liu, and X.-J. Liu, Topological Spin Texture in a Quantum Anomalous Hall Insulator, *Phys. Rev. Lett.* **113**, 136403 (2014).
- [71] H. M. Price, O. Zilberberg, T. Ozawa, I. Carusotto, and N. Goldman, Measurement of Chern numbers through center-of-mass responses, *Phys. Rev. B* **93**, 245113 (2016).
- [72] S. Vajna and B. Dóra, Topological classification of dynamical phase transitions, *Phys. Rev. B* **91**, 155127 (2015).
- [73] Y. Hu, P. Zoller, and J. C. Budich, Dynamical Buildup of a Quantized Hall Response from Nontopological States, *Phys. Rev. Lett.* **117**, 126803 (2016).
- [74] J. C. Budich and M. Heyl, Dynamical topological order parameters far from equilibrium, *Phys. Rev. B* **93**, 085416 (2016).
- [75] J. H. Wilson, J. C. W. Song, and G. Refael, Remnant Geometric Hall Response in a Quantum Quench, *Phys. Rev. Lett.* **117**, 235302 (2016).
- [76] M. Heyl, Dynamical quantum phase transitions: a review, *Rep. Prog. Phys.* **81**, 054001 (2018).
- [77] M. Heyl, Dynamical quantum phase transitions: a brief survey, *Europhys. Lett.* **125**, 26001 (2019).
- [78] H. Hu, B. Huang, E. Zhao, and W. V. Liu, Dynamical Singularities of Floquet Higher-Order Topological Insulators, *Phys. Rev. Lett.* **124**, 057001 (2020).
- [79] H. Hu and E. Zhao, Topological Invariants for Quantum Quench Dynamics from Unitary Evolution, *Phys. Rev. Lett.* **124**, 160402 (2020).
- [80] W.-T. Kuo, D. Arovas, S. Vishveshwara, and Y.-Z. You, Decoherent quench dynamics across quantum phase transitions, *SciPost Phys.* **11**, 084 (2021).
- [81] D.-H. Cai and W. Yi, Synthetic topology and floquet dynamic quantum phase transition in a periodically driven raman lattice, *Phys. Rev. A* **105**, 042812 (2022).
- [82] L. Zhang, L. Zhang, S. Niu, and X.-J. Liu, Dynamical classification of topological quantum phases, *Sci. Bull.* **63**, 1385 (2018).
- [83] L. Zhang, L. Zhang, and X.-J. Liu, Characterizing topological phases by quantum quenches: A general theory, *Phys. Rev. A* **100**, 063624 (2019).
- [84] J. Ye and F. Li, Emergent topology under slow nonadiabatic quantum dynamics, *Phys. Rev. A* **102**, 042209 (2020).
- [85] W. Jia, L. Zhang, L. Zhang, and X.-J. Liu, Dynamically characterizing topological phases by high-order topological charges, *Phys. Rev. A* **103**, 052213 (2021).
- [86] L. Li, W. Zhu, and J. Gong, Direct dynamical characterization of higher-order topological phases with nested band inversion surfaces, *Sci. Bull.* **66**, 1502 (2021).
- [87] L. Zhang, W. Jia, and X.-J. Liu, Universal topological quench dynamics for \mathbb{Z}_2 topological phases, *Sci. Bull.* **67**, 1236 (2022).
- [88] P. Fang, Y.-X. Wang, and F. Li, Generic theory of characterizing topological phases under quantum slow dynamics, *Phys. Rev. A* **106**, 022219 (2022).
- [89] W. Sun, C.-R. Yi, B.-Z. Wang, W.-W. Zhang, B. C. Sanders, X.-T. Xu, Z.-Y. Wang, J. Schmiedmayer, Y. Deng, X.-J. Liu, S. Chen, and J.-W. Pan, Uncover Topology by Quantum Quench Dynamics, *Phys. Rev. Lett.* **121**, 250403 (2018).
- [90] M. Tarnowski, F. N. Ünal, N. Fläschner, B. S. Rem, A. Eckardt, K. Sengstock, and C. Weitenberg, Measuring topology from dynamics by obtaining the Chern number from a linking number, *Nat. Commun.* **10**, 1728 (2019).
- [91] C.-R. Yi, L. Zhang, L. Zhang, R.-H. Jiao, X.-C. Cheng, Z.-Y. Wang, X.-T. Xu, W. Sun, X.-J. Liu, S. Chen, and J.-W. Pan, Observing Topological Charges and Dynamical Bulk-Surface Correspondence with Ultracold Atoms, *Phys. Rev. Lett.* **123**, 190603 (2019).
- [92] Y. Wang, W. Ji, Z. Chai, Y. Guo, M. Wang, X. Ye, P. Yu, L. Zhang, X. Qin, P. Wang, F. Shi, X. Rong, D. Lu, X.-J. Liu, and J. Du, Experimental observation of dynamical bulk-surface correspondence in momentum space for topological phases, *Phys. Rev. A* **100**, 052328 (2019).
- [93] T. Xin, Y. Li, Y.-a. Fan, X. Zhu, Y. Zhang, X. Nie, J. Li, Q. Liu, and D. Lu, Quantum Phases of Three-Dimensional Chiral Topological Insulators on a Spin Quantum Simulator, *Phys. Rev. Lett.* **125**, 090502 (2020).
- [94] W. Ji, L. Zhang, M. Wang, L. Zhang, Y. Guo, Z. Chai, X. Rong, F. Shi, X.-J. Liu, Y. Wang, and J. Du, Quantum Simulation for Three-Dimensional Chiral Topological Insulator, *Phys. Rev. Lett.* **125**, 020504 (2020).
- [95] J. Niu, T. Yan, Y. Zhou, Z. Tao, X. Li, W. Liu, L. Zhang, H. Jia, S. Liu, Z. Yan, Y. Chen, and D. Yu, Simulation of higher-order topological phases and related topological phase transitions in a superconducting qubit, *Sci. Bull.* **66**, 1168 (2021).
- [96] B. Chen, S. Li, X. Hou, F. Ge, F. Zhou, P. Qian, F. Mei, S. Jia, N. Xu, and H. Shen, Digital quantum simulation of floquet topological phases with a solid-state quantum simulator, *Photon. Res.* **9**, 81 (2021).
- [97] D. Yu, B. Peng, X. Chen, X.-J. Liu, and L. Yuan, Topological holographic quench dynamics in a synthetic frequency dimension, *Light Sci. Appl.* **10**, 209 (2021).
- [98] J.-H. Zhang, B.-B. Wang, F. Mei, J. Ma, L. Xiao, and S. Jia, Topological optical raman superlattices, *Phys. Rev. A* **105**, 033310 (2022).
- [99] S. R. Manmana, S. Wessel, R. M. Noack, and A. Muramatsu, Strongly Correlated Fermions after a Quantum Quench, *Phys. Rev. Lett.* **98**, 210405 (2007).
- [100] A. Polkovnikov, K. Sengupta, A. Silva, and M. Vengalattore, Colloquium: Nonequilibrium dynamics of closed interacting quantum systems, *Rev. Mod. Phys.* **83**, 863 (2011).
- [101] T. Kiendl and F. Marquardt, Many-Particle Dephasing after a Quench, *Phys. Rev. Lett.* **118**, 130601 (2017).
- [102] L. Zhang, L. Zhang, Y. Hu, S. Niu, and X.-J. Liu, Nonequilibrium characterization of equilibrium correlated quantum phases, *Phys. Rev. B* **103**, 224308 (2021).
- [103] M. Moeckel and S. Kehrein, Interaction Quench in the Hubbard Model, *Phys. Rev. Lett.* **100**, 175702 (2008).
- [104] L. Han and C. A. R. Sá de Melo, Evolution from BCS to BEC superfluidity in the presence of spin-orbit coupling, *Phys. Rev. A* **85**, 011606(R) (2012).

- [105] M. S. Foster, M. Dzero, V. Gurarie, and E. A. Yuzbashyan, Quantum quench in a $p + ip$ superfluid: Winding numbers and topological states far from equilibrium, *Phys. Rev. B* **88**, 104511 (2013).
- [106] Y. Dong, L. Dong, M. Gong, and H. Pu, Dynamical phases in quenched spin-orbit-coupled degenerate fermi gas, *Nat. Commun.* **6**, 1 (2015).
- [107] I. V. Gornyi, A. D. Mirlin, and D. G. Polyakov, Interacting electrons in disordered wires: Anderson localization and low-T transport, *Phys. Rev. Lett.* **95**, 206603 (2005).
- [108] J. Eisert, M. Friesdorf, and C. Gogolin, Quantum many-body systems out of equilibrium, *Nat. Phys.* **11**, 124 (2015).
- [109] N. Y. Yao, A. C. Potter, I.-D. Potirniche, and A. Vishwanath, Discrete Time Crystals: Rigidity, Criticality, and Realizations, *Phys. Rev. Lett.* **118**, 030401 (2017).
- [110] S. Peotta, F. Brange, A. Deger, T. Ojanen, and C. Flindt, Determination of Dynamical Quantum Phase Transitions in Strongly Correlated Many-Body Systems Using Loschmidt Cumulants, *Phys. Rev. X* **11**, 041018 (2021).
- [111] W. Jia, Z.-H. Huang, X. Wei, Q. Zhao, and X.-J. Liu, Topological superfluids for spin-orbit coupled ultracold Fermi gases, *Phys. Rev. B* **99**, 094520 (2019).
- [112] P. D. Powell, G. Baym, and C. A. R. Sá de Melo, Superfluid transition temperature and fluctuation theory of spin-orbit-and Rabi-coupled fermions with tunable interactions, *Phys. Rev. A* **105**, 063304 (2022).
- [113] T. Esslinger, Fermi-Hubbard physics with atoms in an optical lattice, *Annu. Rev. Condens. Matter Phys.* **1**, 129 (2010).
- [114] L. Tarruell and L. Sanchez-Palencia, Quantum simulation of the Hubbard model with ultracold fermions in optical lattices, *C. R. Phys.* **19**, 365 (2018).
- [115] L. Ziegler, E. Tirrito, M. Lewenstein, S. Hands, and A. Bermudez, Correlated Chern insulators in two-dimensional Raman lattices: A cold-atom regularization of strongly coupled four-Fermi field theories, *Phys. Rev. Res.* **4**, L042012 (2022).
- [116] L. Ziegler, E. Tirrito, M. Lewenstein, S. Hands, and A. Bermudez, Large-N Chern insulators: Lattice field theory and quantum simulation approaches to correlation effects in the quantum anomalous Hall effect, *Ann. Phys.* **439**, 168763 (2022).
- [117] E. Tirrito, S. Hands, and A. Bermudez, Large-S and tensor-network methods for strongly-interacting topological insulators, *Symmetry* **14**, 799 (2022).
- [118] H. Guo and S.-Q. Shen, Topological phase in a one-dimensional interacting fermion system, *Phys. Rev. B* **84**, 195107 (2011).
- [119] B. Song, C. He, S. Niu, L. Zhang, Z. Ren, X.-J. Liu, and G.-B. Jo, Observation of nodal-line semimetal with ultracold fermions in an optical lattice, *Nat. Phys.* **15**, 911 (2019).
- [120] Y.-J. Lin, K. Jiménez-García, and I. B. Spielman, Spin-orbit-coupled Bose-Einstein condensates, *Nature* **471**, 83 (2011).
- [121] P. Wang, Z.-Q. Yu, Z. Fu, J. Miao, L. Huang, S. Chai, H. Zhai, and J. Zhang, Spin-Orbit Coupled Degenerate Fermi Gases, *Phys. Rev. Lett.* **109**, 095301 (2012).
- [122] R. A. Williams, M. C. Beeler, L. J. LeBlanc, K. Jiménez-García, and I. B. Spielman, Raman-Induced Interactions in a Single-Component Fermi Gas Near an s -Wave Feshbach Resonance, *Phys. Rev. Lett.* **111**, 095301 (2013).
- [123] T. L. Gilbert, A phenomenological theory of damping in ferromagnetic materials, *IEEE Trans. Magn.* **40**, 3443 (2004).
- [124] L. Zhang, L. Zhang, and X.-J. Liu, Dynamical detection of topological charges, *Phys. Rev. A* **99**, 053606 (2019).